Wrinkled and cracked amorphous carbon film for high-performance flexible strain sensors

Jingyuan Zhou [a,b], Peng Guo [b,*], Li Cui [b], Chunliang Yan [b], Dan Xu [c], Fali Li [c], Cheng Zhang [a], Aiying Wang [b,*]

[a] International Sci. & Tech. Cooperation Base of Energy Materials and Application, College of Chemical Engineering, Zhejiang University of Technology, Hangzhou 310014, China
[b] Key Laboratory of Marine Materials and Related Technologies, Zhejiang Key Laboratory of Marine Materials and Protective Technologies, Ningbo Institute of Materials Technology and Engineering, Chinese Academy of Sciences, Ningbo 315201, China
[c] CAS Key Laboratory of Magnetic Materials and Devices, Ningbo Institute of Materials Technology and Engineering, Chinese Academy of Sciences, Ningbo 315201, China

ABSTRACT

Due to the trade-off relationship between sensitivity and strain range (ε), it has been a lasting challenge to develop flexible strain sensors with both high sensitivity and excellent stretchability. Here, based on the mismatch of mechanical properties between hard amorphous carbon (a-C) films and soft polydimethylsiloxane (PDMS) substrates, we successfully fabricated a high-performance a-C/PDMS sensor by introducing wrinkled and cracked structure, with the facile direct-current magnetron sputtering technology. The sensor showed a maximum gauge factor of over 2300, high stretchability up to 50 % together with good linearity, rapid response (loading delay time $\tau_1 = 125.4$ ms and unloading delay time $\tau_2 = 51.8$ ms, 0–10 % strain) and excellent repeatability beyond 11,000 cycles. The combined in situ characterization of surface morphology and electrical potential revealed that increasing the applied strain would stimulate the formation of wrinkles and cracks in a-C films, which subsequently favor the cyclic break/contact changes in conductive areas in the surface and film growth direction. This continuous and rapid response of electric resistance would benefit the ultrasensitive and highly stretchable a-C/PDMS sensor. Current insights into the multi-scale and high-precision in situ characterization of a-C films will provide a new strategy to fabricate the flexible strain sensor by using the wrinkled and cracked structure engineering.

1. Introduction

With the rapid development of flexible and wearable electronic devices, advanced carbon materials, such as carbon nanotubes (CNTs), graphite, graphene and carbon black, are drawing increasing attention as sensitive materials, due to their high electrical conductivity, good biocompatibility, excellent chemical and thermal stability. [1–5] Especially, with optimized device structures, those carbon-based flexible sensors can break through the trade-off restriction between sensitivity and strain range (ε) of common flexible sensors, exhibiting both high sensitivity (gauge factor GF > 100) and good stretchability ($\varepsilon > 50$ %). [1,6–10] For example, Li et al. fabricated a core-sheath structural strain sensor based on the hybrid system composing of polyurethane yarn, multilayer graphene nanosheets/thin gold film/graphene nanosheets, and polydimethylsiloxane (PDMS) wrapping layer. The sensor exhibited a GF of 661.59, good stability with an applied strain of 50 %. [11] In addition, Xu et al. developed a multifunctional strain sensor by incorporating the CNTs and MXene onto a porous PDMS sponge, which behaved a wide sensing range (105 % strain) and high sensitivity (GF of 1939). [12] Nevertheless, synthesis of these sensitive carbon-based materials with high performance are quite difficult and complex to the good compatibility with traditional flexible strain sensor process for mass-production, which inhibit their widespread applications to a great extent. [13,14]

Different with the crystallized member of carbon family like CNT and graphene, amorphous carbon (a-C) is a non-crystalline type semiconductor material, with sp^2 bonded (graphite-like) carbon clusters embedded in an sp^3 bonded carbon (diamond-like) matrix. Moreover,

the a-C films with large uniformity can be easily obtained by various physical/chemical vapor deposition (PVD/CVD) techniques under low temperature, enabling it more promising as the alternative coating for polymers. So far, various a-C films have been deposited on highly stretched polymer substrates [15–17], where the integrated flexible strain sensors based on a-C could display a high GF in range of 746.7–1071, a large ε value to 50 % and superior fatigue resistance. However, the trade-off restriction between GF and ε still exists in most instances. If one keeps in mind of the large diversity between hard a-C films and soft polymers, the wrinkles and cracks are inevitably formed in a-C films coated PDMS during deposition and later stretching test. [18–20] Meanwhile, due to the complexity and variety of atomic bonds in a-C films, the sensitivity mechanism of integrated sensor upon the evolution of wrinkles and cracks has not been addressed clearly yet, which may in turn limit the development of high-performance flexible sensors based on a-C. [21] Therefore, it is of great significance and challenging to develop a facile strategy for high-performance amorphous carbon-based flexible sensors, and to in-depth investigate their micro and nano processing under various strains.

In situ characterization of structural evolution during stretching process is a key for understanding the sensitivity mechanism related to topography and electronic behavior of a-C/PDMS integrated sensors. In particular, in situ Raman microscopy together with confocal laser scanning microscopy (CLSM) can be employed to monitor the change of atomic bonds and wrinkles as well as cracks formed in a-C films. Meanwhile, based on the contact potential difference in work function between a conducting atomic force microscope tip and the sample, in situ Kelvin probe force microscopy (KPFM) can be used to reveal the charge distribution, which is dependent upon formed conductive paths on the film surface during strain loading and unloading process. [22–25] These characterization techniques are used to address the in-situ microstructure, morphology and surface potential evolution in a-C films and to clarify the corresponding sensitivity mechanism.

In this work, we deposited hydrogen free a-C films on the soft PDMS substrate by using the direct-current (DC) magnetron sputtering technology, and the flexible a-C/PDMS sensors with GaIn liquid metal was fabricated as the four-electrode structure. Noted that different with the rigid silver paste used in our previous work [15], the gallium-based liquid metal was preferred as electrode here, due to its excellent capability of keeping high electrical conductivity and easy deformation with soft substrate even under the high stretch condition. [26] The sensor performances including sensitivity, stretchability, linearity, hysteresis behavior, stability and repeatability were studied. To elucidate the sensitive mechanism of a-C/PDMS sensor, the interfacial and surface evolution of wrinkles and cracks, and the charge distribution in a-C films under various strains were investigated, with the combination of in situ multiscale and high precision characterization methods involving the Raman spectroscopy, confocal laser scanning microscopy and KPFM.

2. Experimental

2.1. Preparation of a-C films

The hydrogen free a-C films were deposited on PDMS substrates (thickness of 200 μm) by using a DC magnetron sputtering system with a rectangular graphite target of 99.9 % purity. The substrate-target distance was kept at 10 cm and the base pressure of chamber was vacuumed $<1.6 \times 10^{-5}$ Torr. Before deposition, to remove the surface contamination and obtain high adhesion, the PDMS substrates were all etched by Ar^+ plasma for 20 min, with a pulsed bias voltage of -400 V and a working pressure of 8 mTorr. Then, the Ar precursor was introduced to the chamber to ignite the graphite target with a DC sputtering power of 0.9 kW and a working pressure of 1.6 mTorr for a-C deposition. Noted that the floating state without extra bias was applied to the substrate during deposition for obtaining the controlled residual stress in a-C films. [15,27–29] N-type (100) Si was also used as substrate for

comparison. The deposition time was set at 160 min to ensure the 360 ± 10 nm thickness of a-C films. Fig. 1(a) shows the schematic for a-C deposition, and the details can be referred in our previous work. [15,30]

2.2. Fabrication of the a-C/PDMS sensor

The dimension of the a-C/PDMS sensor was 40 mm × 20 mm (length × width), the effective coated area was about 30 mm × 10 mm. Pt wires were subsequently connected to the prepared a-C/PDMS sensors by using the gallium-based liquid metal as conductive electrodes. Specifically, the liquid metal was composed of a mixed mass ratio with gallium, indium, and tin (purity of 99.99 %) at 67.5:21.5:10. The mixture was then heated and stirred for 30 min to obtain liquid metal Galinstan (Ga68.2, In21.8, Sn10) under the protection of nitrogen gas at 60 °C. Galinstan at a mass ratio of 17:3 and copper particles (3–5 μm) were used to increase viscosity. Then, the electrodes on both sides were encapsulated with 3 M insulating tapes. Noted that different with the traditional conductive silver used as electrode [15], the liquid metal was preferred in this work not only to reduce contact resistance for its high electrical conductivity, but also to provide high deformation tolerance to avoid cracks during stretch test.

2.3. Characterization methods of a-C film and a-C/PDMS sensor

The cross-sectional and surface morphologies of a-C films were obtained by a field emission scanning electron microscopy (FEI Quanta FEG 250, USA). A Raman spectrometer (Renishaw in Via-reflex, UK) was used to analyze the atomic bonds of a-C films at a wavelength of 532 nm with acquisition time of 10 s. The relative sp^2/sp^3 content was determined by an X-ray photoelectron spectroscopy (XPS, Axis ultradld, Japan) using the monochromatic Al Kα source. The energy resolution of the XPS system was 0.6 eV. The binding energy was calibrated with C 1s peak at 284.6 eV. The microstructure of the deposited a-C film was characterized by the high-resolution transmission electron microscopy (HRTEM, Tecnai F20, US) with operating voltage 200 kV, and the Focused Ion Beam (FIB) instrument (Carl Zeiss, Auriga) was employed to prepare the samples for the TEM observation.

To evaluate the sensing properties of the a-C/PDMS sensor, the strain was applied with a computer-controlled material testing machine (Instron 5943, USA). The corresponding electrical resistance was calculated based on the electrical current from current source device (Keithley 237, USA) and the voltage measured by voltmeter (Keithley 6517A, USA). The sensitivity, linearity, hysteresis and repeatability of the sensor were tested under an atmospheric environment during stretch process.

During in situ investigation, the atomic bonds of the a-C film and morphologies of the formed wrinkles/cracks were monitored by in situ Raman Microscopy (LabRAM Odyssey, Japan) and laser scanning confocal microscopy (LSM700, Germany), respectively (Fig. S1) (Supplementary information). Moreover, Fig. 1(b) shows the Scanning Probe Microscope (Dimension ICON, Bruker, USA) instrument for the in situ AFM and KPFM measurements. The surface potential (SP) images in KPFM were recorded using Pt—Ir coated silicon cantilevers, and the NanoScope Analysis 1.7 software was used for image processing.

3. Results and discussion

3.1. Microstructure of a-C film

Fig. 2 shows the surface morphology of a-C film deposited on PDMS and Si substrate for comparison. As shown in Fig. 2(a) and (b), the a-C film coated on Si displayed a very smooth and dense surface without any macro-particles, where the clear interface of cross section image presented the thickness about 360 nm. However, different from the feature on rigid Si substrate, many random cracks emerged on the surface of a-C coated PDMS, as shown in Fig. 2(c), which might be attributed to the release of compressive residual stress about 0.5 GPa in a-C films (Fig. S2)
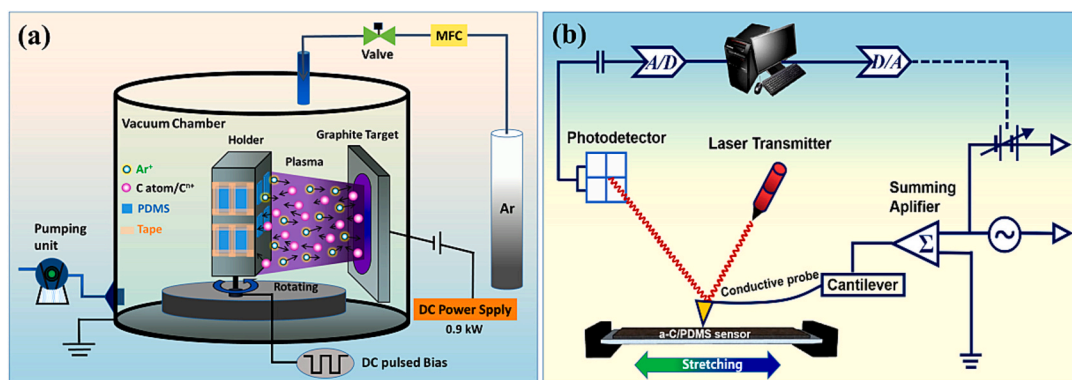
Fig. 1. (a) Schematic diagram of DC magnetron sputtering system for a-C film deposition on PDMS, and (b) schematic illustration of in situ KPFM test during stretch process of a-C/PDMS.
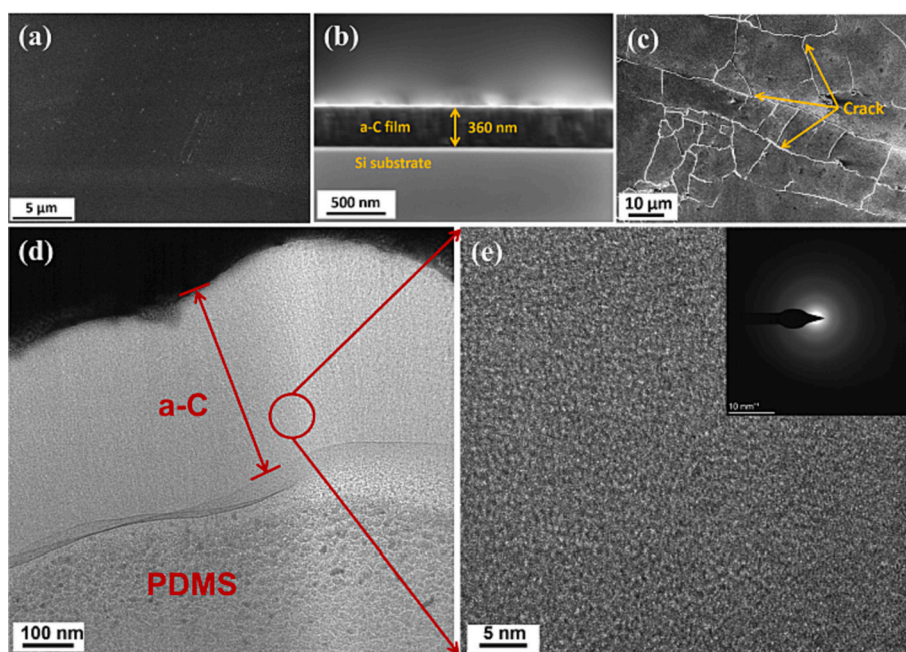

Fig. 2. SEM images of (a) top view and (b) cross-sectional image of a-C film deposited on Si substrate. (c) Surface morphology of a-C film coated on PDMS substrate. (d) HRTEM image and (e) corresponding SAED of a-C/PDMS.
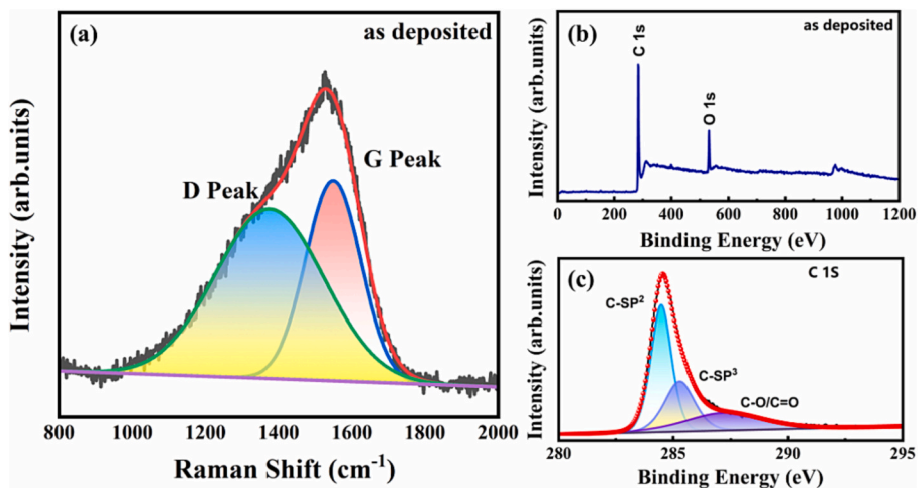

Fig. 3. (a) Raman spectra with the typically deconvoluted D-peak and G-peak, (b) XPS survey spectra and (c) high resolution XPS of C1s peaks with fitted sp^2, sp^3 and C-O/C=O hybridizations for as-deposited a-C film.

(Supplementary Information). Noted that there was no film spallation from PDMS substrate, implying a high adhesion strength between a-C film and PDMS. These results could also be confirmed by the HRTEM and the corresponding selected area electron diffraction (SAED) pattern for a-C film deposited on PDMS substrate, as shown in Fig. 2(d) and (e). The a-C film presented the dense and uniformity structure with a thickness around 360 nm, in which only the characteristics of amorphous granular morphology with diffuse ring shown in the SAED were observed. Although the very small size of polycrystalline graphitic cluster might be distributed in the amorphous matrix, the current resolution of TEM instrument was not enough to characterize this refined structure further.

To address the atomic bond and chemical composition of a-C film, the visible Raman spectroscopy and XPS were further performed. As shown in Fig. 3(a), a broad Raman peak was presented in the range of 800–2000 cm^{-1}, which was the typical characteristic of amorphous carbon films. The peaks could be deconvoluted to two peaks of D-peak at 1380 cm^{-1} and G-peak at 1560 cm^{-1}, [31–33] where the D peak was related to the disordered fine C-sp^2 bond originating from the breathing vibration of the carbon rings, [34] while the G peak was arisen from the C-sp^2 clusters corresponding to the stretching vibration both of carbon rings and the C—C bonds in carbon chains. Fig. 3(b-c) shows the XPS and C 1s spectra of the a-C film deposited on Si substrate. It indicated that only C and a small amount of O were detected, where the O element was possibly due to the residual oxygen in the vacuum chamber during deposition. [35] The carbon peak was deconvoluted into three chemical states, namely sp^2, sp^3 and C-O/C=O hybridizations centred at 284.5, 285.3 and 287.2 eV, respectively. [33–35] According to the ratio of integrating peak area between sp^2 and sp^3, the hybridized sp^2 content in amorphous carbon matrix were deduced around 63.2 % with the neglect of residual oxygen.
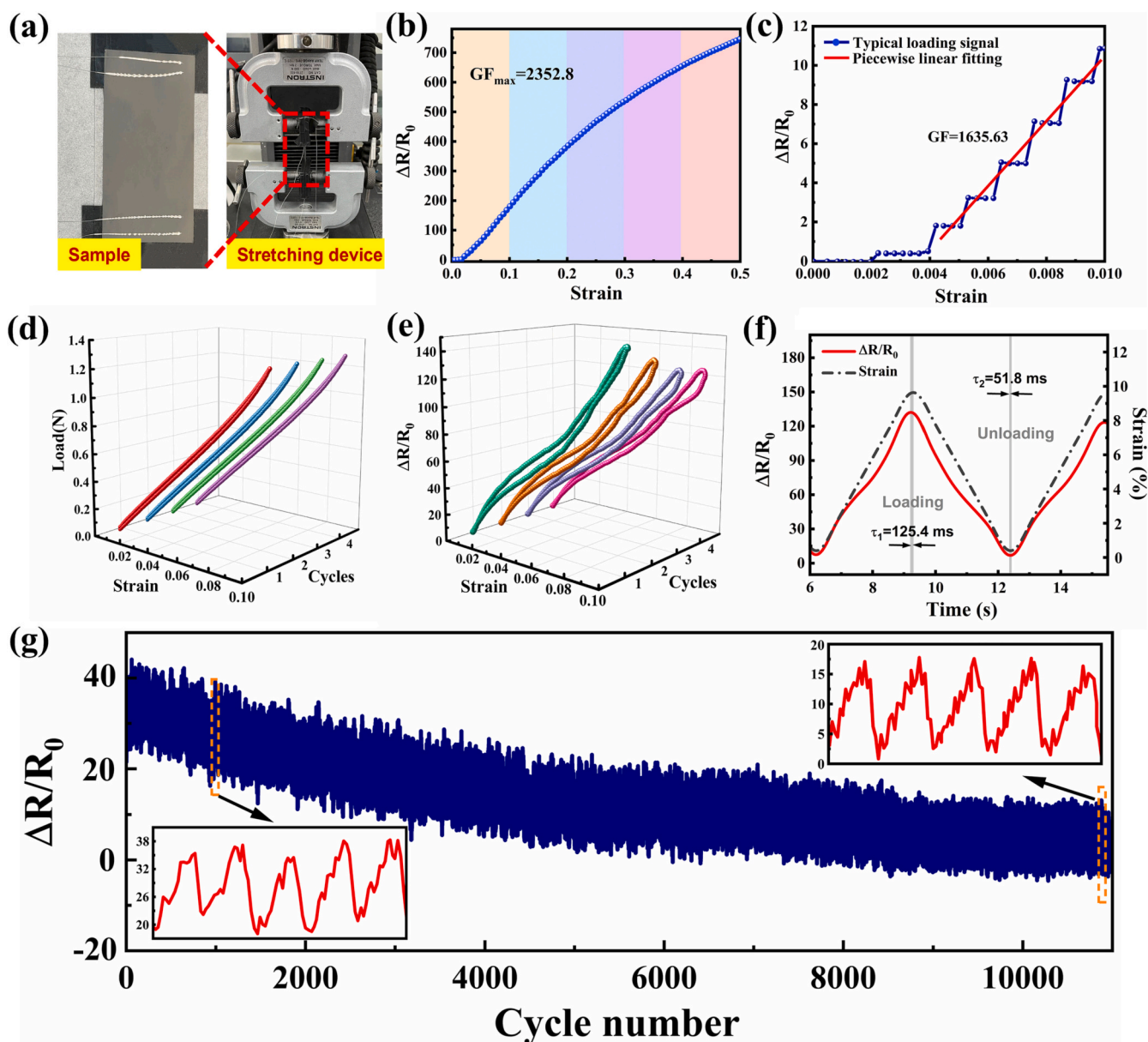

Fig. 4. Electrical performance test results. (a) Photos of test sample and devices, GF test results (b) with 0 to 50 % strain, (c) with 0 to 1 % strain and the piecewise linear fitting. (d) Load-strain curve of sample for four cycles. (e) Hysteresis performance of sensor for four cycles. (f) Response time measurement. Relative change in resistance (black) of sensor was cycled between 0 and 10 % sinusoidal strain (red) at a strain speed of 1 mm s^{-1}. (g) Stability of the relative change in resistance of sensor during 11,000 cycles under 5 % strain. The insets present stable reproducibility for different stretching-releasing cycles (950–955, 10,950–10,955).

3.2. Sensing properties

Fig. 4(a) shows the home-made GF testing device for sensors by addressing the electrical performance. The real-time resistance during test was calculated by the four-point method. The dependence of relative resistance ($\Delta R/R_0$) of integrated a-C/PDMS sensor upon the applied strain was presented in Fig. 4(b). The sensitivity of the sensor during stretching is usually expressed by gauge factor (GF), which is calculated by the following formula [36,37].

$$GF = \frac{\Delta R/R_0}{\varepsilon} \tag{1}$$

where ΔR is the resistance change under loading, R_0 is the original value (280 kΩ in this work), and ε is the strain. Increasing the strain from 0 to 50 % led to remarkable increase of $\Delta R/R_0$, in which five linear-like stages were assigned to the fitted slope with corresponding GF value at 2008.8 ($\varepsilon < 10$ %), 2024.3 (10 % $< \varepsilon <$ 20 %), 1532.9 (20 % $< \varepsilon <$ 30 %), 1180.4 (30 % $< \varepsilon <$ 40 %) and 899.5 (40 % $< \varepsilon <$ 50 %), respectively. In particular, the obtained maximum GF is at 2352.8 with the strain range of 10–15 %. Furthermore, as presented in Fig. 4(c), as the strain varied within a rather small range from 0.2 % to 1 %, the sensor GF reached up to 1635.63 and illustrated well linear performance, implying good capability of a-C/PDMS sensor for monitoring both micro and large tensile strains with high sensitivity. As summarized in Table S1 (Supplementary Information), compared with several reported carbon-based flexible sensors, this a-C/ PDMS flexible strain sensor exhibited a large measurement range to 0.5 and a high GF over 899, simultaneously.

To determine the repeatability of a-C/PDMS sensor, the dependence of tensile stress and sensitivity upon the tensile strain with different test cycles and strain ranges was performed. Fig. 4(d) shows the representative load-strain curves within four test cycles at a constant strain of 10 %, no distinct hysteresis was observed for all the curves with cycle changes, proposing the negligible hysteresis of the fabricated a-C/PDMS sensor. In addition, the stability of a-C/PDMS sensor based on the hysteresis with different stretched strains can be evaluated by following equation [38]:

$$DH = \frac{A_{loading} - A_{unloading}}{A_{loading}} \times 100\% \tag{2}$$

where DH is defined as the sensor hysteresis, $A_{loading}$ and $A_{unloading}$ are the integrated area of loading and unloading response curves, respectively. As shown in Fig. 4(e), the DH of fabricated a-C/PDMS sensor was almost 9.71 % on average with an applied strain of 10 %, and this low hysteresis characteristic could be caused by the superior viscoelasticity of PDMS [26]. To determine the sensor's response time, we applied 10 % strain on sensor at a strain speed of 1 mm s^{-1} and the response time was obtained by calculating the time lag between resistance and strain curves. As demonstrated in Fig. 4(f), the loading and unloading delay time in one cycle were approximately 125.4 ms and 51.8 ms, respectively, which could be sufficient to meet the requirements of human motion detection [37,39]. Fig. 4(g) presents the dynamic response of sensor during 11,000 continuous stretching-releasing cycles under 5 % strain without showing any obvious fatigue, and the insets present stable reproducibility for different stretching-releasing cycles (950–955, 10,950–10,955). It was found that the sensor showed a quite stable response after 11,000 cycles test, and the homologous waveforms also demonstrated a good uniformity. The corresponding video is presented in real-time (Video S1) (Supplementary Information). Meanwhile, with the same applied strain, the insets of Fig. 4(g) presented that the resistance signal kept similar amplitude and waveform at different stages, implying a good repeatability of the sensor.

3.3. In situ characterization of a-C/PDMS sensor

Fig. 5(a) shows the in situ Raman spectra of a-C films deposited on PDMS substrate under various applied strains. Although the tensile strain was changed from 0 to 50 %, all the spectra illustrated the typical characteristic of amorphous carbon film and no obvious changes occurred for the peak density. Since the carbon Raman spectroscopy could be deconvoluted to G peak at 1560 cm^{-1} and D peak at 1380 cm^{-1}, it is known empirically that the structural variation of a-C films can be estimated according to the G peak position, the area ratio of D peak and G peaks (I_D/I_G), as well as the full width at half maximum of G peak (G-FWHM). [40] The graphitic sp^2 content will increase with shifting upwards of G peak position and the sp^2 cluster size will increase with the increase of I_D/I_G, while the smaller G-FWHM replies the increase of structural disorder in a-C matrix. [41] As shown in Fig. 5(b), when the tensile strain increased from 0 to 50 %, both the G-peak position and I_D/I_G increased firstly and then showed a decrease tendency after 25 % strain, while the G-FWHM exhibited an opposite tend. This result essentially indicated that increasing the stretched strain from 0 to 25 % may lead to the increase of sp^2 content and sp^2 cluster size.

When uniaxial tension was applied, a number of mutually parallel channel cracks and wrinkles can be easily introduced into a-C/PDMS. Fig. 6 shows the in situ morphologies of a-C/PDMS sensor during the initial 3 test circles, from unstrained state to applied strain up to 50 %. Compared to the pristine state without strain (Fig. S3) (Supplementary Information), the first loading cycle with the applied strain of 10 % resulted in many tiny cracks on surface at 45$\overset{\circ}{}$ along the tensile direction, as shown in Fig. 6(a-1). Further increasing the strain to 30 % (Fig. 6(a-2)) favored the increase of size and density of cracks, and stimulated the formation of new wrinkles along the tensile direction. In this case, the wrinkles could make the break area along the cracks easily contact with each other to decrease the resistance. When the stretched strain reached to the maximum value of 50 %, as shown in Fig. 6(a-3), the cracks and wrinkles behaved similar to those of 30 % strain case, while the size of cracks increased significantly. Different with the loading process, Fig. 6 (a-4) and (a-5) illustrated that unloading strain of 30 % and 10 % caused the slight fade of formed cracks and wrinkles. Noted that once the unstrained state was recovered, many new tiny cracks emerged on the surface of the a-C films, which was quite different from that of the initial as-deposited samples. Fig. 6(b) and (c) present the topographies of the a-C films coated on PDMS during the following 2nd and 3rd cycle tests, respectively, where the related cracks and wrinkles performed similar characteristics under the same loading-unloading process, as those in the 1st applied strain cycle. Nevertheless, one should keep eyes on the stability of these restored cracked and wrinkled structures after the unloading process, suggesting a reversible microstructure with the applied strain during various test cycles. The corresponding real-time video based on optical images as expected was also presented in Video S2 (Supplementary Information).

To quantitatively figure out the variation of crack and wrinkle with applied strain from the laser confocal microscopy, the open-source image processing program Image J was used here. As shown in Fig. 7 (a) and (c), both the densities of cracks and wrinkles increased with the tensile strain and presented a similar change trend. In the first cycle, when loaded to 10 %, 30 %, and 50 %, the value of crack density was 61/mm^2, 159/mm^2, and 206/mm^2, respectively. During unloading process, the corresponding crack density under the same applied strain was larger. In the subsequent two loading-unloading cycles, the crack density tended to be stable under certain strain, with an average change rate of only 3.46 %. However, the crack width and the wrinkle area showed good reversibility during each cycle, as shown in Fig. 7(b, d). For example, in Fig. 7(b), when loaded to 10 %, 30 % and 50 % in the third cycle, the average crack width was 6.83 μm, 16.23 μm and 23.88 μm respectively, and decreased to 15.97 μm and 7.03 μm with 30 % and 10 % strain during unloading process, respectively. Only the crack and wrinkle density will increase and cannot be recovered after the first
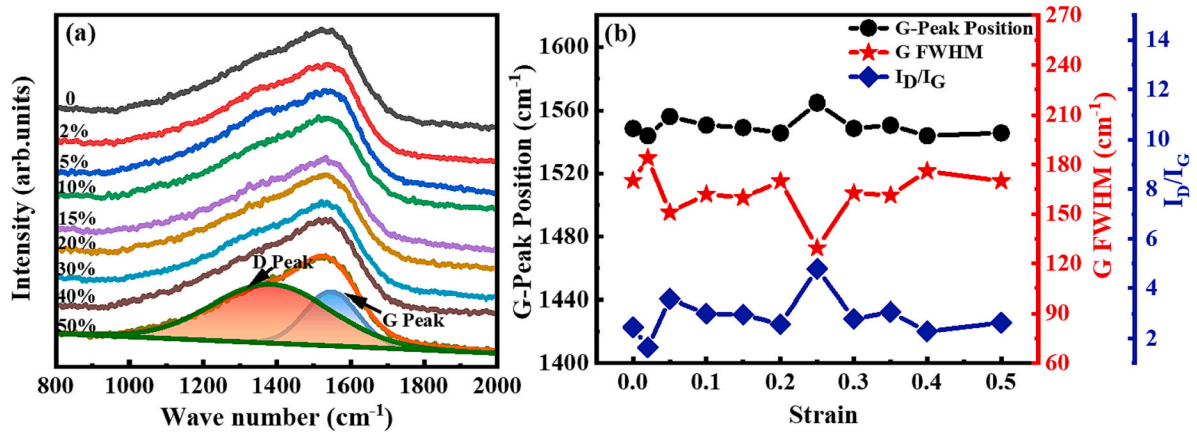
Fig. 5. (a) In-situ Raman spectra, and (b) the fitted G-peak position, G-FWHM and I_D/I_G of a-C on PDMS substrate with various strains.

stretching process. Then in the following two test cycles, the cracks and wrinkles can present relatively identical geometric features under the same applied strain. Table S2 lists the relevant statistics of crack and wrinkle structure of a-C/PDMS sensor under the first three strain cycles.

After the first loading-unloading test cycle, the crack width and the wrinkle area under specific tensile strain will obey certain statistical laws. The statistical distribution of crack width obeyed the generalized-extreme-value (GEV) distribution given by

$$G(x; \mu, \sigma, \xi) = exp\left\{ -\left[1 + \frac{\xi}{\sigma} \cdot (x - \mu) \right]^{-1/\xi} \right\} \tag{3}$$

where x is a random variable, μ, σ and ξ are the location parameter, scale parameter and shape parameter, respectively. And the statistical distribution of the wrinkle area approximately followed the logistic distribution, given by

$$F(\delta) = \frac{1}{1 + e^{-(\delta - \varphi)/\tau}} \tag{4}$$

where δ is a random variable, φ and τ are the location parameter and shape parameter, respectively. As a representative example, Fig. 8(a) and (b) show the crack width histogram, the wrinkle area histogram and the respective distribution fitting curves for the a-C/PDMS sample loaded to 50 % tensile strain in the second cycle. Table S3 and S4 lists the GEV fitting parameters of the crack width and the logistic fitting parameters of the wrinkle area for a-C/PDMS sample, respectively.

Since the PDMS substrate is insulating, it is difficult to use traditional contacting AFM to obtain the surface potential in current work. Therefore, in situ KPFM method is applied to explore the evolution of conductive paths and potential barriers of the wrinkled and cracked structure. Fig. 9 shows the change of surface potentials of a-C/PDMS sensor. Four individual scanning steps (80 μm × 80 μm) were accomplished to address the different process with unstrained, loading within 20 % strain, loading beyond of 40 % strain and unloading state, respectively. Fig. 9(a)-(d) shows the in situ AFM images with tapping mode for samples during loading-unloading process. The tiny cracks and few overlapping structures were observed for unstrained sample in Fig. 9 (a). Further increasing the applied strain from 20 % to 40 % would stimulate the propagation of crack width and formation of new wrinkles, as shown in Fig. 9(b, c). Meanwhile, Fig. 9(d) indicated that these cracks and overlapping structures could be partially recovered after unloading strain process.

Fig. 9(a_1)-(d_1) exhibit the corresponding scanning probe images of a-C/PDMS with various strain states. In general, the voltage was applied to the sample by the Kelvin controller compensating the contact potential difference (V_{CPD}) with the tip grounded. The color of scanning probe image represents the variation of charge carrier density. [42] The

surface potential of sample can be calculated by the formula

$$\Phi_S = \Phi_T - eV_{CPD} \tag{5}$$

where Φ_S and Φ_T are the surface potential of sample and work function of the tip, respectively. [43,44] In addition, Φ_T will remain unchanged over the time of several scans (15 min per scan with at least 2 s for a single line scanning) during un-contact AFM mode. [45,46] Therefore, the brighter contrast of image indicates higher positive voltage and larger V_{CPD} of sample. For comparison, all the overlapping structure with four strain states illustrated brighter KPFM images than other areas, while the cracks area seemed darker in the opposite way. It could be supposed that the overlapping areas exhibited lower potentials and more conductive. As shown in Fig. 9(a_2)-(d_2), the maximum V_{CPD} of overlapping structures under unstrained, loading within strain <10 %, loading with strain beyond 40 % and unloading state was estimated at 136.02 mV, 264.89 mV, 273.22 mV and 191.04 mV, respectively. The tip was coated with Pt—Ir and its Φ_T was 5.4 eV. [47] According to Eq. (5), the Φ_S of overlapping structures under unstrained, loading within strain <10 %, loading with strain beyond 40 % and unloading state were estimated at 5.26 eV, 5.14 eV, 5.12 eV and 5.21 eV, respectively. The Φ_S of the overlapping structures decreased when the sample was loaded with the strain of 40 %, and increased during unloading process. This reduction of Φ_S for 40 % loading strain was possibly attributed to the interaction between adjacent sp^2 clusters and the formation of overlapping structures in amorphous carbon matrix, which finally added the conductive paths between break areas and led to a better conductivity.

3.4. Sensing mechanisms

The ultrasensitive and highly stretchable performance of the fabricated a-C/PDMS sensor could be explained in terms of the change in conductive paths with the applied strains. Fig. 10 presents the dependence of flexible sensing upon the schematic evolution of cracked and wrinkled structures during loading-unloading process. Different with the a-C films coated on rigid Si substrate, the tiny cracks were formed when the hard a-C film (hardness of 14.4 GPa, residual stress of 0.5 GPa, as shown in Fig. S4 and Fig. S2 of Supplementary Information) was deposited on flexible PDMS substrate. When a strain <10 % was applied to the sample, the soft PDMS would deform easily along the tensile direction, while the brittle a-C could not withstand this deformation. To dissipate the stretched strain energy, initial tiny cracks on a-C were propagated and more cracks appeared along the two-dimensional surface plane. This led to the break of conductive paths and improved the electric resistance rapidly, which favored the high GF and sensitive property of fabricated a-C/PDMS sensor.

In generally, increasing the strain continuously would cause high-density cracks and high resistance quickly. Such phenomena played a
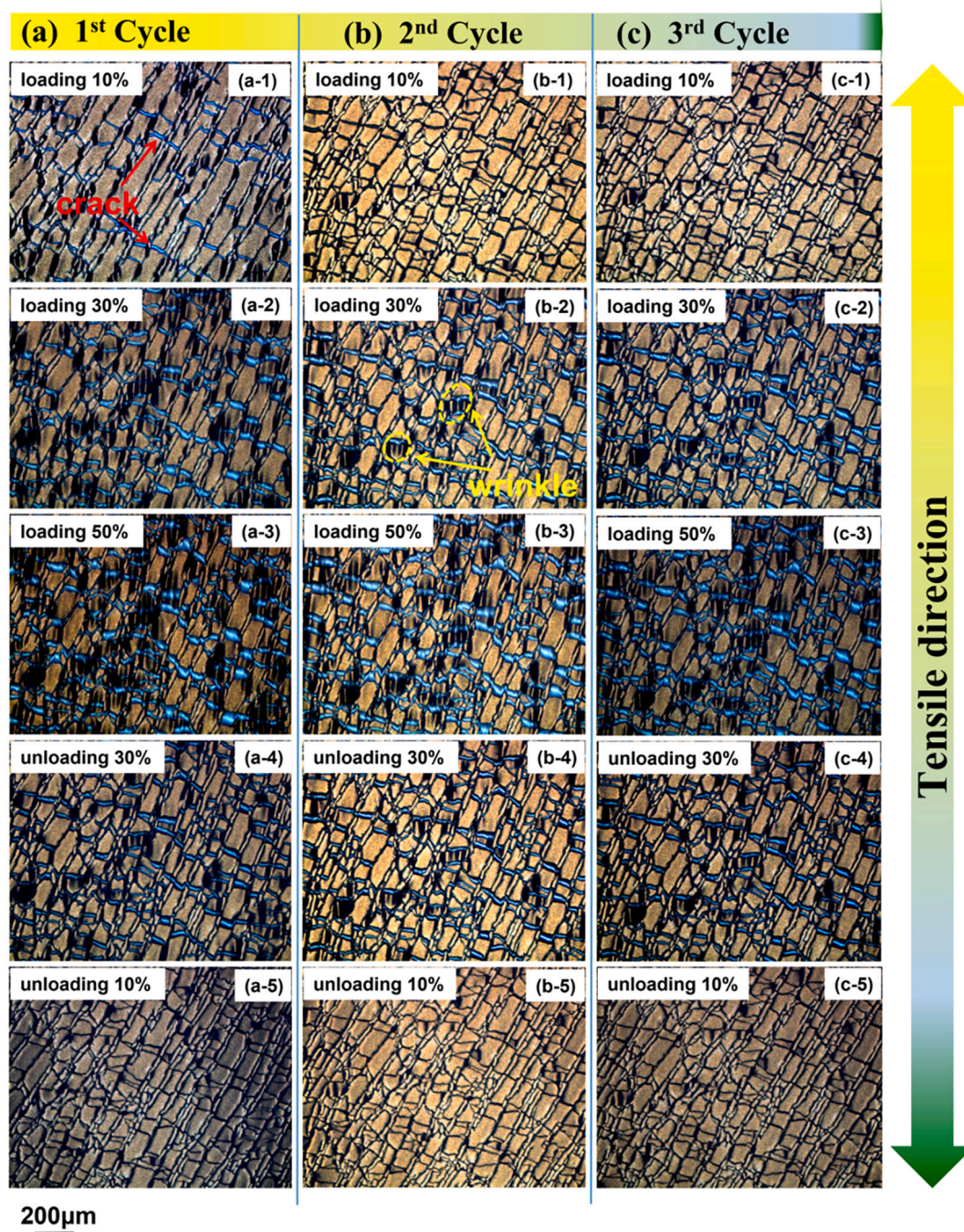
Fig. 6. In situ CLSM illustrates that the cracks and wrinkles in a-C film can change differently with applied strain during the initial 3 loading-unloading test cycles. (a) 1st cycle, (b) 2nd cycle, (c) 3rd cycle.

key role in the traditional trade-off relationship between the sensitivity and strain range. For the a-C/PDMS sensor fabricated in this work, increasing the applied strains to 50 % would generate more cracks, stimulate the appearance of larger longitudinal cracks in a-C matrix, and produce more wrinkles due to Poisson effect of the PDMS substrate and the strong adhesion between hard a-C film and soft PDMS. Subsequently, some of the broken conductive areas were overlapped by contacting with each other along the vertical plane direction, generating new conductive paths with more lower surface potential regions. Particularly, the atomic band structure of a-C films was changed in the strain range of 20–30 %, in which the maximum value of sp^2 content and sp^2 cluster size were achieved at the strain of 25 % as revealed by in situ Raman and KPFM test. As a result, such cracked and wrinkled structures

together with the combination of conductive paths in three-dimensional direction benefited the excellent performance of a-C/PDMS sensor with the maximum GF of 2352.8 and tensile strain of 10 %–15 %. However, further enlarging the strain beyond of 25 % would lead to the elongate growth of more cracks and decrease the capability of restored inclined cracks, corresponding to the slightly deterioration of a-C/PDMS sensor performance as expected.

Finally, it was noticed that, due to the capability of retaining high transverse shrinkage and minimizing the problem of hysteresis for used PDMS substrate, the fractured regions occurred in the a-C films could easily overlap and contact with each other both along the two-dimensional plane and out of surface plane. This made the great contribution to the increased connecting bridge between broken areas
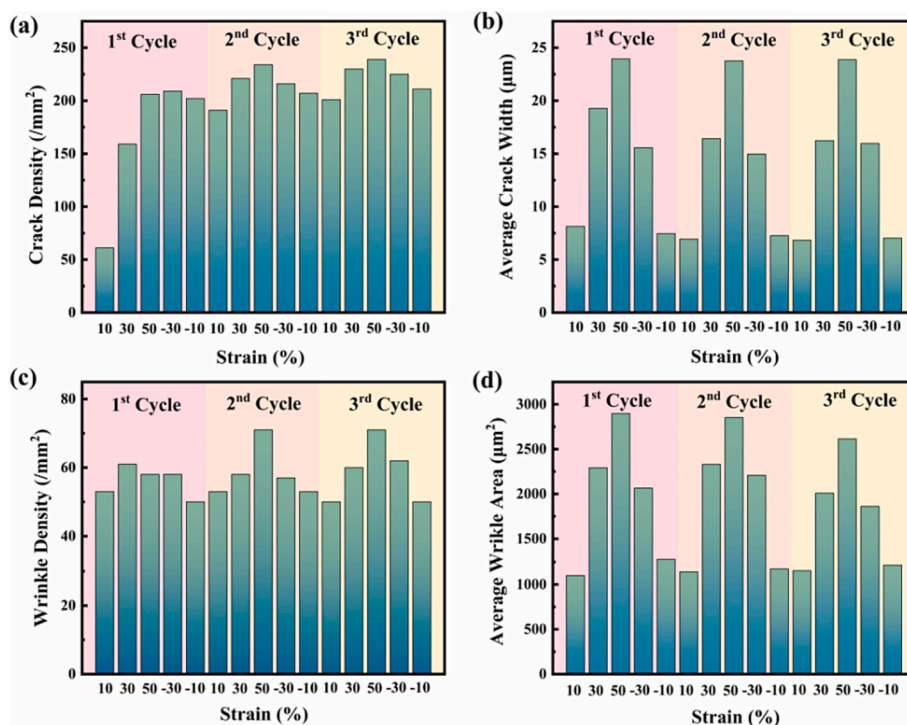
Fig. 7. Evolutions of crack and wrinkle distributed in the a-C/PDMS sample as a function of applied strains during the initial three loading-unloading cycle. (a) crack density, (b) average crack width, (c) wrinkle density, and (d) average wrinkle area.
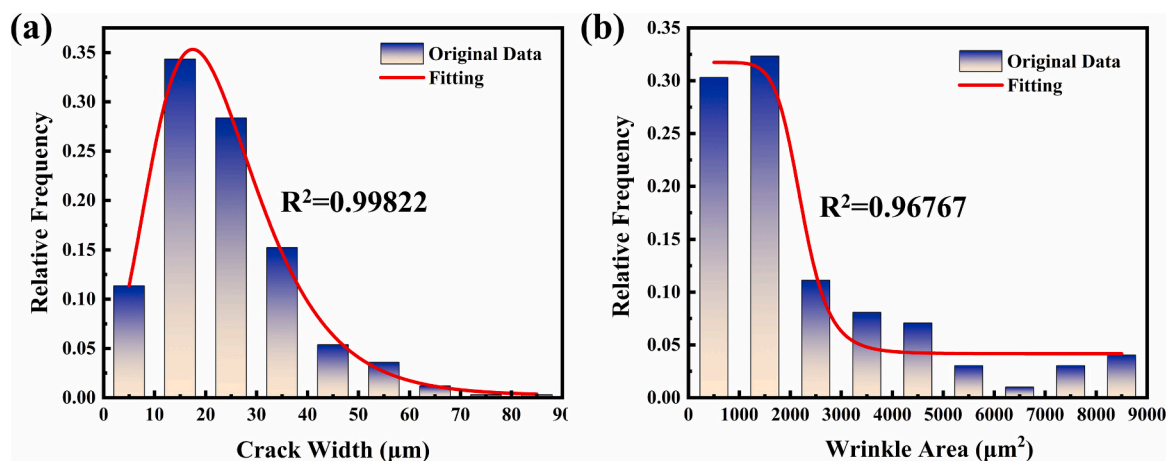

Fig. 8. Distributions and fitting results of (a) crack width and (b) wrinkle area as function of relative frequency with loaded 50 % strain at 2nd cycle.

and the partial generation of new conductive paths, which subsequently promoted the high sensitivity and superior stretchability as well as the repeatability of our fabricated a-C/PDMS sensor.

4. Conclusion

In summary, amorphous carbon-based stretchable strain sensor was fabricated by using a facile direct-current magnetron sputtering technology and the combined capability of flexible PDMS substrate. The a-C/ PDMS sensor showed an ultrasensitive and highly stretchable performance with maximum gauge factor of 2352.8, high stretchability up to 50 %, low hysteresis and fast response time, excellent repeatability beyond 11,000 cycles with good linearity. In particular, the a-C/PDMS sensor enabled the possibility to both monitor the small strain <0.2 % and the extensively large strain to 50 % with high sensitivity. The comprehensive in situ characterization of surface morphology and

electrical potential by Raman, CLSM and KPFM test revealed that increasing the applied strain would stimulate the formation and elongate degradation of wrinkles and cracks in a-C matrix. Moreover, the dramatic variety emerged in the atomic bond of a-C films during loading-unloading strain process, where the maximum value of sp^2 content and sp^2 cluster size serving as conductive phases were demonstrated under the stretched strain of 25 %. As a result, different with the traditional trade-off strategy, such continuous changes and the rapid responses of electric resistance finally benefited the ultrasensitive and highly stretchable compatibility in our fabricated a-C/PDMS sensor together with good repeatability.

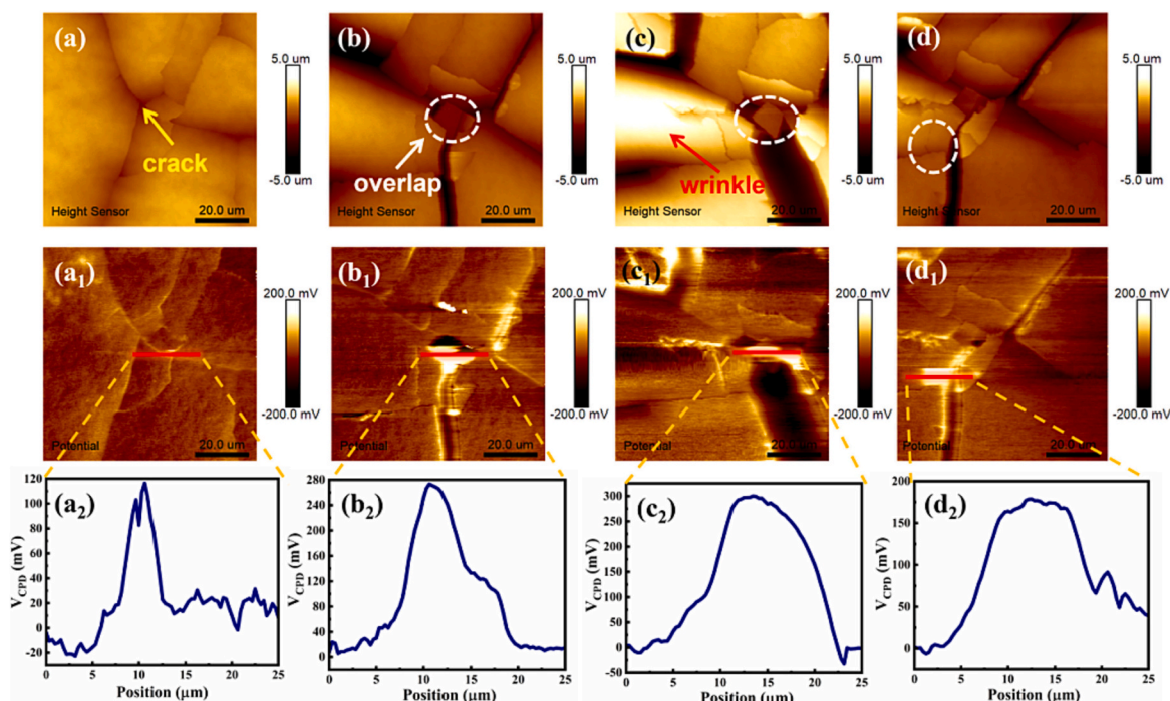Supplementary data to this article can be found online at https://doi.org/10.1016/j.diamond.2022.109619.

Fig. 9. In situ KPFM reveals the changes for surface potential of cracks area and overlapping areas in a-C film under different tensile strains. (a)-(d) In situ tapping mode AFM images, (a₁)-(d₁) the corresponding KPFM potential images of a-C/PDMS, and (a₂-d₂) profiles of V_{CPD}. Noted that (a, a₁, a₂) is unstrained, (b, b₁, b₂) is loaded within 20 % strain, (c, c₁, c₂) is loaded over 40 % strain, and (d, d₁, d₂) is unloading process.
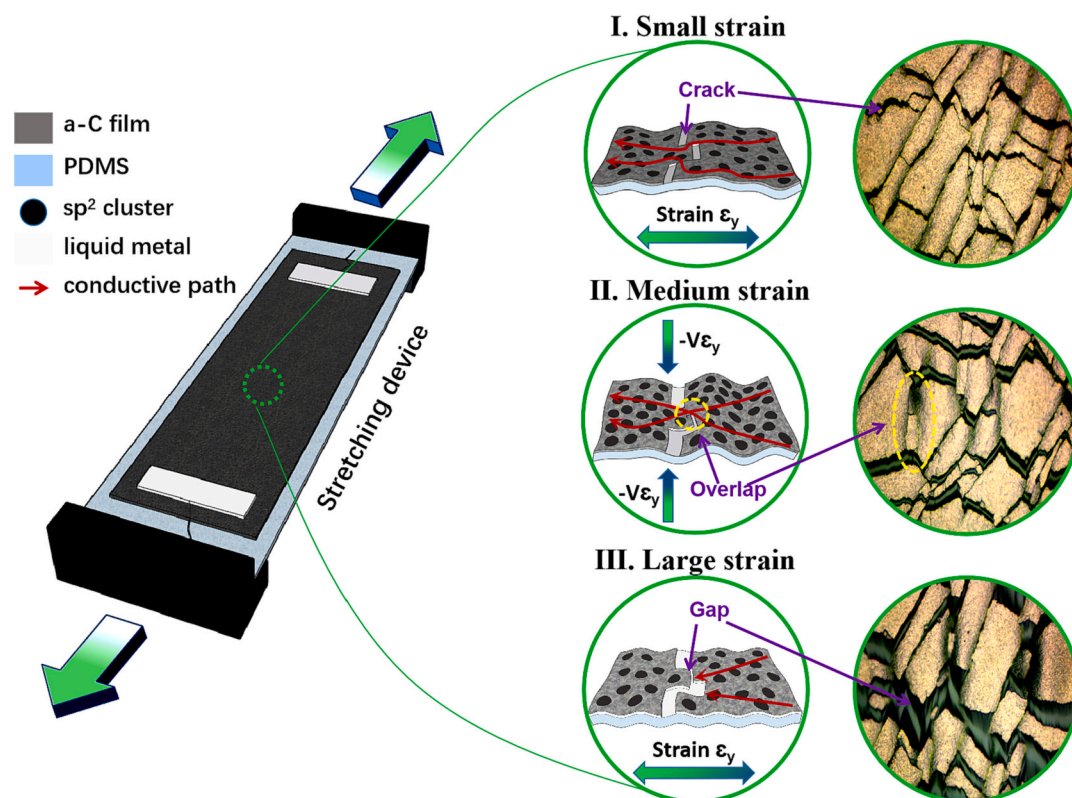

Fig. 10. Schematic of the flexible sensing mechanism in a-C films coated on PDMS.

CRediT authorship contribution statement

Jingyuan Zhou: Conceptualization, Validation, Formal analysis, Investigation, Data curation, Writing - original draft, Visualization.

Peng Guo: Conceptualization, Investigation, Writing - review & editing, Visualization, Project administration, Funding acquisition. **Li Cui:** Project administration, Writing - review & editing, Funding acquisition. **Chunliang Yan:** Software, Investigation. **Dan Xu:** Software, Data

References

[1] S. Shajari, S. Ramakrishnan, K. Karan, L.J. Sudak, U. Sundararaj, Ultrasensitive wearable sensor with novel hybrid structures of silver nanowires and carbon nanotubes in fluoroelastomer: multi-directional sensing for human health monitoring and stretchable electronics, Appl. Mater. Today 26 (2022), 101295.

[2] H. Liu, H. Zhang, W. Han, H. Lin, R. Li, J. Zhu, et al., 3D printed flexible strain sensors: from printing to devices and signals, Adv. Mater. 33 (2021) 2004782.

[3] X. Gong, K. Huang, Y. Wu, X. Zhang, Recent progress on screen-printed flexible sensors for human health monitoring, Sens. Actuator A: Phys. 345 (2022), 113821.

[4] J. Zhang, M. Wang, Z. Yang, X. Zhang, Highly flexible and stretchable strain sensors based on conductive whisker carbon nanotube films, Carbon 176 (2021) 139–147.

[5] L. Liu, X. Zhang, D. Xiang, Y. Wu, D. Sun, J. Shen, et al., Highly stretchable, sensitive and wide linear responsive fabric-based strain sensors with a self-segregated carbon nanotube (CNT)/Polydimethylsiloxane (PDMS) coating, Prog. Nat. Sci.: Mater. Int. 32 (2022) 34–42.

[6] C.M. Das, L. Kang, Q. Ouyang, K. Yong, Advanced low-dimensional carbon materials for flexible devices, InfoMat. 2 (2020) 698–714.

[7] D. Joo, M. Kang, S.J. Park, S. Yu, W. Park, Fabrication method of flexible strain sensors with CNTs and solvents, Sens. Actuator A: Phys. 345 (2022), 113775.

[8] L. Liu, Z. Jiao, J. Zhang, Y. Wang, C. Zhang, X. Meng, et al., Bioinspired, superhydrophobic, and paper-based strain sensors for wearable and underwater applications, ACS Appl. Mater. Interfaces 13 (2021) 1967–1978.

[9] W. Liu, Q. Chen, Y. Huang, D. Wang, L. Li, Z. Liu, In situ laser synthesis of pt nanoparticles embedded in graphene films for wearable strain sensors with ultra-high sensitivity and stability, Carbon 190 (2022) 245–254.

[10] H. Sun, K. Dai, W. Zhai, Y. Zhou, J. Li, G. Zheng, et al., A highly sensitive and stretchable yarn strain sensor for human motion tracking utilizing a wrinkle-assisted crack structure, ACS Appl. Mater. Interfaces 11 (2019) 36052–36062.

[11] X. Li, K. Koh, M. Farhan, K. Lai, Ultraflexible polyurethane yarn-based wearable strain sensor with polydimethylsiloxane infiltrated multilayer sheath for smart textiles, Nanoscale 12 (2020) 4110.

[12] B. Xu, F. Ye, R. Chen, X. Luo, G. Chang, R. Li, A wide sensing range and high sensitivity flexible strain sensor based on carbon nanotubes and MXene, Ceram. Int. 48 (2022) 10220–10226.

[13] Z. Wang, B. Chen, S. Sun, L. Pan, Y. Gao, Maskless formation of conductive carbon layer on leather for highly sensitive flexible strain sensors, Adv. Electron. Mater. 6 (2020) 2000549.

[14] X. Chen, X. Zhang, D. Xiang, Y. Wu, C. Zhao, H. Li, et al., 3D printed high-performance spider web-like flexible strain sensors with directional strain recognition based on conductive polymer composites, Mater. Lett. 306 (2022), 130935.

[15] X. Ma, Q. Zhang, P. Guo, X. Tong, Y. Zhao, A. Wang, Residual compressive stress enabled 2D-to-3D junction transformation in amorphous carbon films for stretchable strain sensors, ACS Appl. Mater. Interfaces 12 (2020) 45549–45557.

[16] B. Wang, Y. Jiang, R. Zhao, G. Liu, A. He, J. Gao, Piezoresistive effect observed in flexible amorphous carbon films, J. Phys. D. Appl. Phys. 51 (2018), 175304.

[17] P. Xue, C. Chen, D. Diao, Ultra-sensitive flexible strain sensor based on graphene nanocrystallite carbon film with wrinkle structures, Carbon 147 (2019) 227–235.

[18] M. Alam, N. Mukherjee, S. Ahmed, Electron field emission property of nanostructure wrinkle thin film induced by amorphous diamond like carbon, Mater. Today: Proc. 5 (2018) 2082–2088.

[19] W. Kaczorowski, K. Gajewski, W. Szymanski, D. Batory, A. Wojciechowska, L. Swiatek, et al., Evaluation of mechanical properties of carbon coatings synthesised in radio frequency plasma on PDMS, Surf. Coat. Technol. 333 (2018) 220–228.

[20] S. Nagashima, T. Hasebe, D. Tsuya, T. Horikoshi, M. Ochiai, S. Tanigawa, et al., Controlled formation of wrinkled diamond-like carbon (DLC) film on grooved poly (dimethylsiloxane) substrate, Diam. Relat. Mater. 22 (2012) 48–51.

[21] S. Nagashima, H. Ebrahimi, K.R. Lee, A. Vaziri, M.W. Moon, Tunable nanochannels fabricated by mechanical Wrinkling/Folding of a stiff skin on a soft polymer, Adv. Mater. Interfaces 2 (2015) 1400493.

[22] E.M. Alexeev, N. Mullin, P. Ares, H. Nevison-Andrews, O. Skrypka, T. Godde, et al., Emergence of highly linearly polarized interlayer exciton emission in MoSe2/WSe2 heterobilayers with transfer-induced layer corrugation, ACS Nano 14 (2020) 11110–11119.

[23] S. Kumar, D. Chaudhary, N. Khare, Enhanced thermoelectric figure of merit in Bi2Te3-CNT-PEDOT nanocomposite by introducing conducting interfaces in Bi2Te3 nanostructures, APL Mater. 7 (2019), 081123.

[24] A. Ruiz, N. Seoane, S. Claramunt, A. Garciá-Loureiro, M. Porti, C. Couso, et al., Workfunction fluctuations in polycrystalline TiN observed with KPFM and their impact on MOSFETs variability, Appl. Phys. Lett. 114 (2019), 093502.

[25] J. Čermák, T. Yamada, K. Ganzerová, B. Rezek, Doping effects and grain boundaries in thermal CVD graphene on recrystallized cu foil, Adv. Mater. Interfaces 3 (2016) 1600166.

[26] Y. Wu, Y. Zhou, W. Asghar, Y. Liu, F. Li, D. Sun, et al., Liquid metal-based strain sensor with ultralow detection limit for human–machine interface applications, Adv. Intell. Syst. 3 (2021) 2000235.

[27] J. Wei, P. Guo, L. Liu, H. Li, H. Li, S. Wang, et al., Tailored electrochemical behavior of ta-C film by glancing angle deposition, Appl. Surf. Sci. 516 (2020), 146115.

[28] X. Li, S. Xu, P. Ke, A. Wang, Thickness dependence of properties and structure of ultrathin tetrahedral amorphous carbon films: a molecular dynamics simulation, Surf. Coat. Technol. 258 (2014) 938–942.

[29] S. Xu, X. Li, M. Huang, P. Ke, A. Wang, Stress reduction dependent on incident angles of carbon ions in ultrathin tetrahedral amorphous carbon films, Appl. Phys. Lett. 104 (2014), 141908.

[30] X. Ma, X. Tong, P. Guo, Y. Zhao, Q. Zhang, H. Li, et al., MEMS piezo-resistive force sensor based on DC sputtering deposited amorphous carbon films, Sens. Actuator A: Phys. 303 (2020), 111700.

[31] A. Ito, A. Takayama, S. Saito, H. Nakamura, Formation and classification of amorphous carbon by molecular dynamics simulation, Jpn. J. Appl. Phys. 52 (2013) 01AL04.

[32] H. Li, T. Xu, J. Chen, H. Zhou, H. Liu, The effect of applied dc bias voltage on the properties of a-C: H films prepared in a dual dc–rf plasma system, Appl. Surf. Sci. 227 (2004) 364–372.

[33] P. Guo, X. Li, L. Sun, R. Chen, P. Ke, A. Wang, Stress reduction mechanism of diamond-like carbon films incorporated with different Cu contents, Thin Solid Films 640 (2017) 45–51.

[34] W.A. Eurídice, N.B. Leite, R.V. Gelamo, P.A.A. Buranello, M.V. Silva, C.J. F. Oliveira, et al., A-C: H films produced by PECVD technique onto substrate of Ti6Al4V alloy: chemical and biological responses, Appl. Surf. Sci. 15 (2020), 144084.

[35] V.Yu. Fominski, R.I. Romanov, I.S. Vasil'evskii, D.A. Safonov, A.A. Soloviev, A. A. Ivanov, et al., Pulsed laser modification of layered B-C and mixed BCx films on sapphire substrate, Diam. Relat. Mater. 114 (2021) 108336.

[36] S. Yoon, H. Koo, S. Chang, Highly stretchable and transparent microfluidic strain sensors for monitoring human body motions, ACS Appl. Mater. Interfaces 7 (2015) 27562.

[37] X. Zhang, D. Xiang, Y. Wu, E. Harkin-Jones, J. Shen, Y. Ye, et al., High-performance flexible strain sensors based on biaxially stretched conductive polymer composites with carbon nanotubes immobilized on reduced graphene oxide, Compos. Part A 151 (2021), 106665.

[38] R. Sun, L. Gao, F. Liu, H. Su, L. Wu, Z. Zou, et al., Magnetically induced robust anisotropic structure of multi-walled carbon nanotubes/Ni for high-performance flexible strain sensor, Carbon 194 (2022) 185–196.

[39] N. Hou, Y. Zhao, T. Yuan, L. Li, X. Li, W. Zhang, Flexible multifunctional pressure sensors based on cu-CAT@CNFN and ZnS:Cu/PDMS composite electrode films for visualization and quantification of human motion, Compos. Part A 163 (2022), 107177.

[40] E. Mohagheghpour, M. Rajabi, R. Gholamipour, M. Larijani, S. Sheibani, Correlation study of structural, optical and electrical properties of amorphous carbon thin films prepared by ion beam sputtering deposition technique, Appl. Surf. Sci. 360 (2016) 52–58.

[41] B. Li, Y. Zhang, Z. Wu, Z. Qin, H. Ji, X. Liu, et al., Magnetic properties and corrosion resistance of co-DLC nanocomposite films with different cobalt contents, Diam. Relat. Mater. 117 (2021) 108477.

[42] A.S. Nikolenko, V.V. Strelchuk, P.M. Lytvyn, I.M. Danylenko, S.V. Malyuta, O. G. Gontar, et al., Correlated kelvin-probe force microscopy, micro-FTIR and micro-raman analysis of doping anisotropy in multisectorial boron-doped HPHT diamonds, Diam. Relat. Mater. 124 (2022) 108927.

[43] S. Sadewasser, Sadewasser, Sascha, Glatzel, Nanoscale visualization of hot carrier generation and transfer at non-noble metal and oxide interface, J. Mater. Sci. Technol. 98 (2022) 151–159.

[44] W. Choi, R. Bera, S. Han, H. Park, T. Go, M. Choi, et al., Doping effect of zeolite-templated carbon on electrical conductance and supercapacitance properties, Carbon 193 (2022) 42–50.

[45] Z. Yin, R. He, Y. Chen, Z. Yin, K. Yan, K. Wang, et al., Effects of surface micro-galvanic corrosion and corrosive film on the corrosion resistance of AZ91-xNd alloys, Appl. Surf. Sci. 536 (2021), 147761.

[46] R. Kumar, D. Varandani, B.R. Mehta, Nanoscale interface formation and charge transfer in graphene/silicon Schottky junctions; KPFM and CAFM studies, Carbon 98 (2016) 41–49.

[47] Y. Zhang, J. Zuo, Y. Gao, P. Li, W. He, Z. Zheng, Investigation on the nanoscale electric performance of NiO thin films by C-AFM and KPFM: the effect of Cu doping, J. Phys. Chem. Solids 131 (2019) 27–33.